

Accurate Calculation of Parasitic Capacitance of High Frequency Inductors

Jiangtao TU, Kaining FU, Wei CHEN, and Yanhui QIU

Abstract—High-frequency inductors are important devices in power converters. The parasitic capacitance not only affects the electromagnetic interference suppression effect of filter inductors, but also causes efficiency degradation and other problems. In order to predict the impedance characteristics of high-frequency inductors, this paper proposes a method to accurately calculate the parasitic capacitance of inductors. Firstly, the effect of the winding structure parameters on the electric field distribution between adjacent turns is investigated. Then, the calculation method is optimized, which can be used to accurately describe the electric field distribution. Secondly, the effect of core parasitic capacitance on the total capacitance is further investigated. Finally, a calculation method for the parasitic capacitance of high-frequency inductors is established. In the experiments, the impedance test and finite element simulation are used as references to compare the calculation results. The maximum calculation error is only within 5.05%, which verifies the validity and accuracy of the proposed calculation method.

Index Terms—Electric field distribution, finite element simulation, inductors, parasitic capacitance.

I. INTRODUCTION

WITH the increasing switching frequency, the electromagnetic parameters design of magnetic components has become a major bottleneck limiting the power converter to further increase the switching frequency and power density [1]–[2]. This is because the parasitic parameters of magnetic components cause high-frequency voltage oscillations, which not only lead to higher EMI noise, but also reduce the efficiency of the power converter [3]–[4]. More and more

researchers are focusing on the high-frequency parasitic parameters characterization of magnetic components [5].

As shown in Fig. 1, the high-frequency model of the inductor contains the inductance L , the parasitic capacitance C_p , and the equivalent parallel resistance R_s . It can be found that accurate measurement or calculation of the parasitic capacitance C_p is essential to accurately predict the high-frequency impedance characteristics of an inductor. Parasitic capacitance C_p contains the capacitance inside the winding and the capacitance between the winding and the core. In addition, the capacitance inside the winding can be categorized into turn-to-turn capacitance and layer-to-layer capacitance. In order to optimize the high-frequency characteristics of inductors at the design level, it is necessary to propose an analytical method for theoretically calculating the parasitic capacitance of inductors. In [6], a theoretical calculation method for parasitic capacitance of single-layer winding is presented. Further, a calculation method for parasitic capacitance of multilayer winding is presented in [7] and used to evaluate the size of parasitic capacitance of transformers and EMI chokes [8]–[9]. However, these methods do not take into account the effect of the parasitic capacitance between the winding and the core on the total capacitance [10]. In addition, the application of these techniques is strictly limited to the distance between the windings and the core, making it difficult to apply them widely [11].

Finite element simulations can be used to analyze the parasitic parameter characteristics under various complex core and winding structures. However, 3D finite element simulation suffers from time-consuming and non-convergence problems due to large mesh sizes and limitations in computer computational resources. As a result, parasitic capacitance is difficult to realize fast prediction by simulation [12]–[13]. In [14], parasitic capacitance of an inductors can be extracted by impedance test. This method cannot be used to predict the size of parasitic capacitance at the design stage. [15] proposed a method to calculate the turn-to-turn capacitance, but the core parasitic capacitance was not studied in depth. This results in a large error between the calculated and measured values. For inductor design, the parasitic capacitance should be reduced as small as possible. Once the winding arrangement of the inductor is determined, the parasitic capacitance can be accurately calculated by the proposed method. Hence, the proposed calculation method can be used to predict the parasitic capacitance of the inductor in the design stage.

This paper is organized as follows. In Section II, the characteristics of the electric field distribution between adjacent

Manuscript received January 22, 2025; revised March 25, 2025; accepted April 14, 2025. Date of publication June 30, 2025; date of current version May 12, 2025. This work was supported in part by National Natural Science Foundation of China under the grant 51777036, Natural Science Foundation of Xiamen, China under the grant 3502Z202372043, and Research start-up fund of Xiamen University of Technology under the grant YKJ23008R. (Corresponding author: Kaining Fu.)

J. Tu and Y. Qiu are with School of Electrical Engineering and Automation, Xiamen University of Technology, Xiamen 361024, China (e-mail: 1092111621@qq.com; 512621898@qq.com).

K. Fu is with Xiamen Key Laboratory of Frontier Electric Power Equipment and Intelligent Control, the School of Electrical Engineering and Automation, Xiamen University of Technology, Xiamen 361024, China (e-mail: fkn@xmut.edu.cn).

W. Chen is with School of Electrical Engineering and Automation, Fuzhou University, Fuzhou 350108, China (e-mail: chw@fzu.edu.cn).

Digital Object Identifier 10.24295/CPSS TPEA.2025.00018

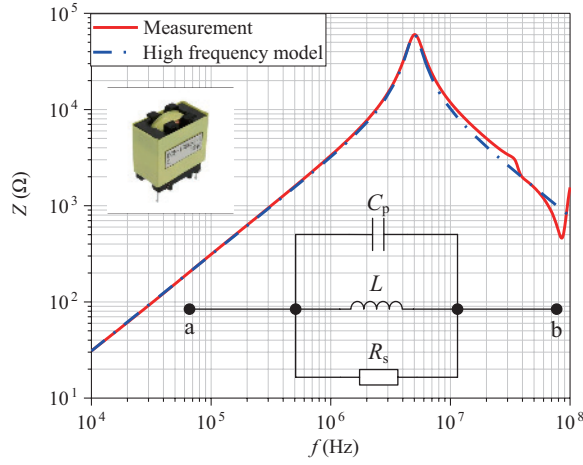


Fig. 1. Equivalent circuit of inductor.

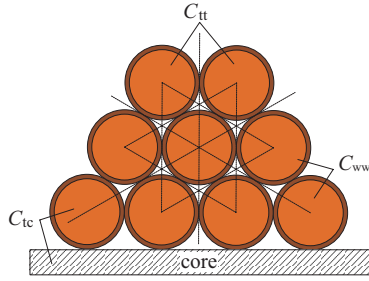


Fig. 2. Cross-section of an inductor with three winding layers.

turns of the winding are explored, and the parasitic capacitance of the windings are deduced using electromagnetic field equations. In Section III, the core parasitic capacitance between winding and core is analyzed and calculated. In Section IV, the calculation model on the description of electric field is further optimized. In Section V, the accuracy of the proposed calculation method is verified by finite element method (FEM) simulation and impedance measurement. Section VI gives the conclusion of this paper.

II. PARASITIC CAPACITANCE MODEL OF WINDING

As illustrated in Fig. 1, the impedance characteristics of the inductor exhibit capacitive impedance after the resonance point due to the presence of parasitic capacitance. For better and clearer understanding the distribution of parasitic capacitance, Fig. 2 shows the cross-section view of an inductor with three layers of windings. The parasitic capacitance consists of the following three components:

1. Turn-to-turn parasitic capacitance in the same layer of the winding (C_{tt});
2. Turn-to-turn parasitic capacitance between adjacent layers of the winding (C_{ww});
3. Parasitic capacitance between winding and core (C_{tc}).

Both turn-to-turn capacitance C_{tt} and C_{ww} are determined by the winding arrangement. This is because the winding arrangement affects the distribution of electric field lines between turns, which in turn affects the size of the parasitic capacitance. The parasitic capacitance between the winding and the core is

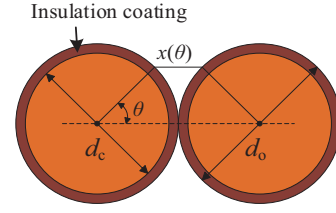


Fig. 3. Cross-section of turn-to-turn.

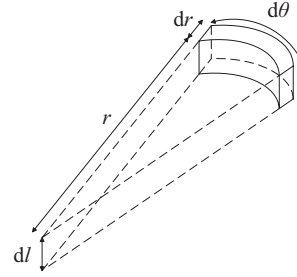


Fig. 4. Insulation coating.

affected not only by the area between the winding and the core, but also by the dielectric properties of the core material.

Fig. 3 shows the cross-section view of the same layer winding, where the windings are densely wound. d_c and d_o are the diameter of bare conductors and conductors with insulation coatings, respectively. $x(\theta)$ is the path of the electric field lines through the air. As can be seen in Fig. 3, the electric field lines between adjacent turns need to pass through the insulating coating and air. Thus, the equivalent parasitic capacitance between the adjacent turns of conductor consists of an insulating coating capacitance and an air capacitance connected in series.

A. Capacitance of Insulation Coating

The unit of insulation coating is shown in Fig. 4, where r is the radius of the bare conductor. The capacitance can be expressed as:

$$dC = \epsilon \frac{dS}{x} \quad (1)$$

Then, the capacitance of the insulation coating can be expressed as:

$$dC = \frac{\epsilon_0 \epsilon_r r}{2dr} d\theta dl \quad (2)$$

where ϵ_r is the relative permittivity of the insulation material.

Combined with (2) and the relevant parameters shown in Fig. 3 and Fig. 4, the capacitance of insulation coatings can be further expressed as:

$$dC_{tc} = \epsilon_0 \epsilon_r d\theta \int_0^l dl \int_{\frac{d_c}{2}}^{\frac{d_o}{2}} \frac{r}{2dr} = \frac{\epsilon_0 \epsilon_r l}{2 \ln \frac{d_o}{d_c}} d\theta \quad (3)$$

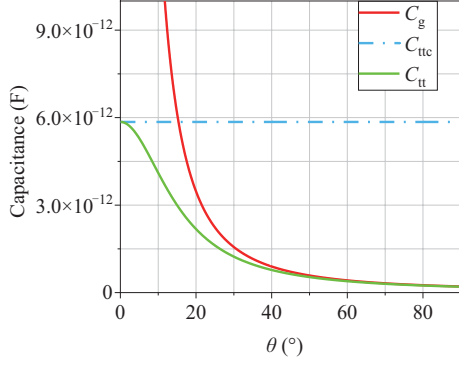


Fig. 5. Capacitance microelement value distribution.

Then, the insulation capacitance can be further simplified as:

$$\frac{dC_{tc}}{d\theta} = \frac{\varepsilon_0 \varepsilon_r l_t}{2 \ln \frac{d_o}{d_c}} \quad (4)$$

B. Air Capacitance

As shown in Fig. 3, assuming that the path of electric field lines in the air is a straight line, the length of the electric field lines at angle θ , $x(\theta)$, can be expressed as:

$$x(\theta) = d_o(1 - \cos \theta) \quad (5)$$

Combined with (1) and (5), the air capacitance can be expressed as:

$$\frac{dC_g(\theta)}{d\theta} = \varepsilon_0 \frac{l_t d_o}{2(1 - \cos \theta)} \quad (6)$$

C. Total Capacitance Between Turn-to-Turn

Since the air capacitance dC_g and the insulation capacitance dC_{tc} are in series connection, the total capacitance between turn-to-turn can be calculated. Combining (4) and (6), the turn-to-turn capacitance at angle θ , can be given as:

$$dC_{tt}(\theta) = \frac{dC_{tc} dC_g}{dC_{tc} + dC_g} = \frac{\varepsilon_0 l_t}{2} \frac{1}{1 + \frac{1}{\varepsilon_r} \ln \left(\frac{d_o}{d_c} \right) - \cos \theta} d\theta \quad (7)$$

Based on (7), the turn-to-turn capacitance C_{tt} can be further calculated as:

$$C_{tt} = \varepsilon_0 l_t \int_0^{\frac{\pi}{2}} \frac{1}{1 + \frac{1}{\varepsilon_r} \ln \left(\frac{d_o}{d_c} \right) - \cos \theta} d\theta \quad (8)$$

where the capacitance C_{tt} is determined not only by the structure parameters but also by the integration range.

Fig. 5 shows the capacitance value at different angles θ , including air capacitance, insulation capacitance, and turn-to-

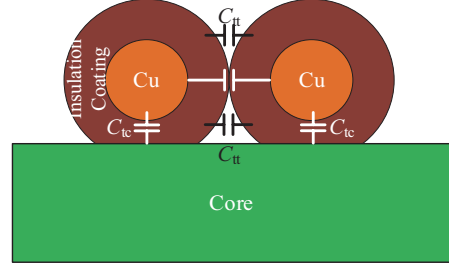


Fig. 6. Parasitic capacitance between winding and core.

turn capacitance. The insulation capacitance remains constant at different θ . Air capacitance C_g is changed versus angle θ . According to (8), the turn-to-turn capacitance C_{tt} is also changed versus angle.

Since the air capacitance in the range of $[30^\circ, 90^\circ]$ is smaller than that in the range of $[0^\circ, 30^\circ]$, the integration range $[0^\circ, 30^\circ]$ is chosen to calculate the capacitance [15].

In order to show the influence of integration range on calculation results, an example is given as following: $d_o=0.3$ mm, $d_c=0.34$ mm, $l_t=47$ mm. The 3D FEM simulation result is used as a reference (The simulated capacitance is 4.6782 pF). For the integration range used in [15], i.e., $[0^\circ, 30^\circ]$, the calculated result is 3.4489 pF, resulting in 26.28% relative error. If the integration range is further extended to $[0^\circ, 90^\circ]$, the calculation result is 4.4654 pF, and the corresponding relative error is reduced to 4.549%.

III. PARASITIC CAPACITANCE BETWEEN WINDING AND CORE

As shown in Fig. 6, there are parasitic capacitances C_{tc} between the winding and the core. If the winding is wound directly on the core without the use of a bobbin, the parasitic capacitance C_{tc} and the turn-to-turn capacitance C_{tt} satisfy: $C_{tc}=2C_{tt}$. However, this assumption can only be applied to magnetic components without bobbin, such as toroidal inductors, and does not apply to magnetic components with bobbins such as EE, EI, and PQ type cores.

Since the winding is wound on a bobbin, the parasitic capacitance between the winding and the core should consider the dielectric effect due to the bobbin. In addition, the presence of bobbin makes the windings to be located at different distances from the core center columns, side columns, and yoke. These factors cause the parasitic capacitance C_{tc} and the winding turn-to-turn capacitance C_{tt} no longer meet the requirements: $C_{tc}=2C_{tt}$.

In order to accurately calculate the parasitic capacitance C_{tc} , a sub-area calculation method is used. As shown in Fig. 7, the parasitic capacitance between the winding and the core can be calculated in three parts:

1. Capacitance between the winding and the core center column (C_{cw1});
2. Capacitance between the winding and the core side column (C_{cw2});
3. Capacitance between the winding and the yoke (C_{cw3}).

The total capacitance C_{cw} between the core and the winding consists of three parts, C_{cw1} , C_{cw2} , and C_{cw3} , which can be expressed as:

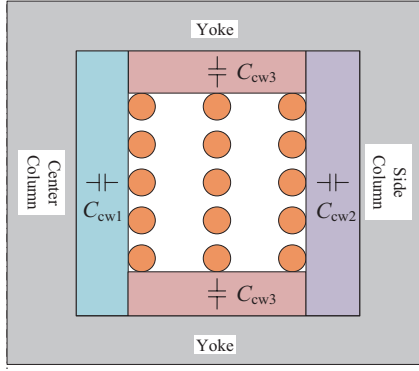


Fig. 7. Capacitance distribution between winding and core.

$$C_{cw} = k_{cw1} \cdot C_{cw1} + k_{cw2} \cdot C_{cw2} + k_{cw3} \cdot C_{cw3} \quad (9)$$

where k_{cw1} , k_{cw2} and k_{cw3} are the normalization factors for the capacitance of each part.

In order to calculate the parasitic capacitance between each part of the core and the winding, the type of core should be considered in detail. The calculation can be done using the parallel plate capacitance formula and the coaxial cylindrical capacitance formula, respectively. They can be expressed as:

$$C_x = \begin{cases} \alpha_x \varepsilon_0 \varepsilon_x \frac{2\pi h_x r_x}{d_x} \\ \alpha_x \varepsilon_0 \varepsilon_x \frac{2\pi h_x}{\ln(1 + \frac{d_x}{r_x})} \end{cases} \quad x = cw1, cw2, cw3 \quad (10)$$

where ε_0 is the vacuum permittivity constant, ε_x is the relative permittivity of the material, h_x and r_x are the height and radius, respectively. d_x is the distance between two plates or coaxial cylindrical plates, and α_x is the weighting factor.

There are two factors that require attention: one is the selection of capacitance formula, and the other is the determination of weighting factor α_{cw2} . For the first factor, the structure type of magnetic core should be considered. For the inductor with an EE core, the calculation formula for parasitic capacitance should be chosen as the parallel plate capacitance formula. For the inductor with a PQ core, the calculation formula for parasitic capacitance should be chosen as the coaxial cylindrical capacitance formula.

For the second factor, the weight factor α_{cw2} should be determined according to type of magnetic core. For PQ-type inductors, the degree of side column enclosure to the windings can be represented by $\alpha_{cw2} = 1/2$. For pot-type inductors, it can be represented by $\alpha_{cw2} = 8/9$. For the EE-type inductor, it can be represented by $\alpha_{cw2} = 1$.

Since the research object is the PQ core, the coaxial cylindrical capacitance formula was chosen for the calculation of the structural capacitance between the winding and core. Fig. 8 shows the identification of the structural parameters for the quantitative calculation of the capacitance between the windings and the core.

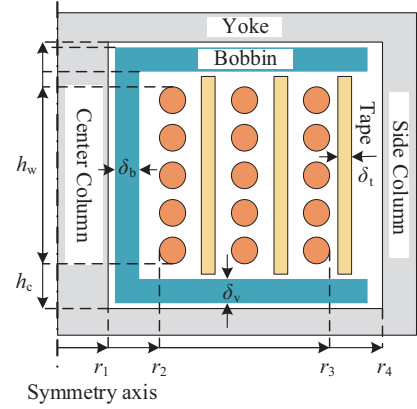


Fig. 8. Structural parameters of inductors.

A. Calculation of C_{cw1}

This part of capacitance refers to the capacitance between the innermost winding and the center column of the core. The dielectric material of the capacitance C_{cw1} is composed by air and bobbin. The relevant parameters can be calculated by the following equation:

$$\begin{cases} \alpha_{cw1} = 1 \\ h_{cw1} = h_c \\ d_{cw1} = r_2 - r_1 + \frac{d_o}{2} \\ r_{cw1} = r_1 + \frac{d_{cw1}}{2} \\ \varepsilon_{cw1} = \frac{\varepsilon_a \varepsilon_b d_{cw1}}{\varepsilon_a \delta_b (r_2 - r_1 - \delta_b)} \end{cases} \quad (11)$$

where ε_{cw1} is the relative permittivity of the composite dielectric made up of the air and the bobbin.

The capacitance C_{cw1} can be calculated by substituting (11) into (10).

B. Calculation of C_{cw2}

This part of capacitance is between the outermost winding and the core side column. As the number of winding layers p increases, the outer radius r_3 of the winding gradually increases, resulting in C_{cw2} becoming non-negligible part of the core capacitance. The relevant parameters can be obtained by the following equations:

$$\begin{cases} h_{cw2} = h_c \\ d_{cw2} = r_4 - r_3 + \frac{d_o}{2} \\ r_{cw2} = r_3 + \frac{d_{cw2}}{2} \\ \varepsilon_{cw2} = \frac{\varepsilon_a \varepsilon_t d_{cw2}}{\varepsilon_a \delta_t + \varepsilon_t (d_{cw2} - \delta_t)} \end{cases} \quad (12)$$

where ε_{cw2} is the relative permittivity of the composite dielectric formed by air and insulation tape.

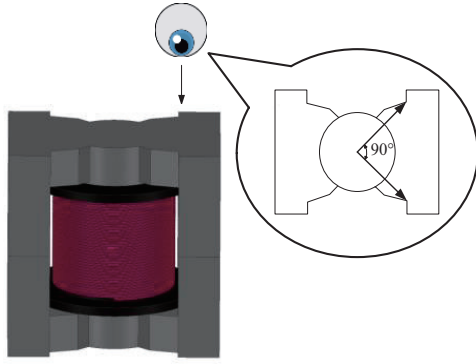


Fig. 9. PQ2625 inductor overhead view.

The weighting factor α_{cw2} in (10) depends on the degree of enclosure of the winding by the side column.

For most cores, the side columns are partially surrounded by the winding, rather than the entire 360° circumference of the winding. Fig. 9 shows an inductor with a PQ magnetic core, where the single side column enclosing the winding at an angle of 90° . Thus, the entire core side column surrounds the winding by 50%. For other types of cores, the weighting factor α_{cw2} need to be determined for specific structures. The parasitic capacitance C_{cw2} can be calculated by substituting (12) into (10).

C. Calculation of C_{cw3}

The capacitance C_{cw3} consists of winding to the top and bottom yokes, respectively. It increases with the number of winding layers p and the wire diameter d_o . The relevant parameters can be calculated by:

$$\left\{ \begin{array}{l} \alpha_{cw3} = 1 \\ A_{cw3} \approx \frac{\pi}{2}(r_3^2 - r_2^2) \\ d_{cw3} = \frac{h_c - h_w}{2} + \frac{d_o}{2} \\ \varepsilon_{cw3} = \frac{\varepsilon_a \varepsilon_b d_{cw3}}{\varepsilon_a \delta_v + \varepsilon_b \left(\frac{h_c}{2} - \frac{h_w}{2} - \delta_v \right)} \end{array} \right. \quad (13)$$

where ε_{cw3} is the relative permittivity of the composite dielectric consisting of air and the bobbin. The parasitic capacitance C_{cw3} between the yoke and the winding can be calculated by substituting (13) into (10).

D. Normalization Factors $k_{cw1}, k_{cw2}, k_{cw3}$

When the leakage inductance is far smaller than the magnetizing inductance, the potential distribution of the winding can be regarded as linearly distributed along the height direction. The calculation process of C_{cw1} will be taken as an example. As shown in Fig. 10, the potential difference between the winding and the core at one terminal is U_{D1} and the potential difference between the winding and the core at the other end is U_{D2} , then the total energy stored in this capacitance can be expressed as:

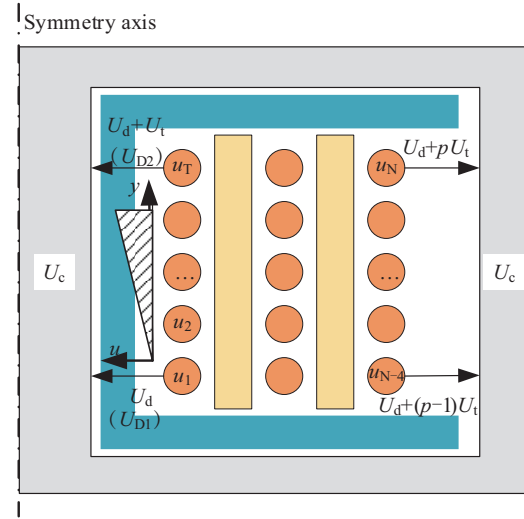


Fig. 10. Inductor winding potential distribution.

$$W = \frac{C_x}{6} (U_{D1}^2 + U_{D1}U_{D2} + U_{D2}^2) \quad (14)$$

The energy stored on the parasitic capacitances C_{cw1} , C_{cw2} and C_{cw3} between each part of the core and the winding can be calculated according to (14), respectively:

$$\left\{ \begin{array}{l} W_{cw1} = C_{cw1} \frac{3U_d^2 + 3U_dU_t + U_t^2}{6} \\ W_{cw2} = C_{cw2} \frac{3U_d^2 + (6p-3)U_dU_t + (3p^2 - 3p + 1)U_t^2}{6} \\ W_{cw3} = C_{cw3} \frac{6U_d^2 + 6pU_dU_t + (2p^2 - p + 1)U_t^2}{6} \end{array} \right. \quad (15)$$

where p is the number of winding layers and U_t is the voltage drop of the innermost layer.

The energy stored in the parasitic capacitance between each part of the core and the winding can be expressed as:

$$W_x = \frac{C_x}{2} (pU_t)^2 \quad x = cw1, cw2, cw3 \quad (16)$$

The Normalization factors $k_{cw1}, k_{cw2}, k_{cw3}$ can be derived from (15) and (16):

$$\left\{ \begin{array}{l} k_{cw1} = \frac{3k_U^2 + 3k_U + 1}{3p^2} \\ k_{cw2} = \frac{3k_U^2 + (6p-3)k_U + (3p^2 - 3p + 1)}{3p^2} \\ k_{cw3} = \frac{6k_U^2 + 6pk_U + (2p^2 - p + 1)}{3p^2} \end{array} \right. \quad (17)$$

where k_U is the core potential factor, which will be analyzed in the following.

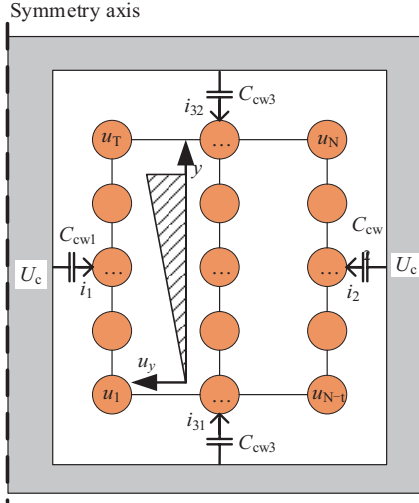


Fig. 11. System equivalent circuits for cores and winding.

E. Core Potential Coefficient

In order to calculate the stored electric energy in the core, the core potential should be solved. As shown in Fig. 11, the potential of each turn of the winding are provided. The calculation of center column capacitance, C_{cw1} , is used as an example. The potentials of the first and last turns of the first layer of the winding are U_1 and U_T , respectively. The potential at the height y of the innermost layer is given by:

$$U_y = U_1 + (U_T - U_1) \frac{y}{h_w} \quad (18)$$

The capacitance between the winding and the core at the height y is:

$$C_y = \alpha_{cw1} \epsilon_0 \epsilon_{cw1} \frac{2\pi dy}{\ln(1 + \frac{d_{cw1}}{r_{cw1}})} \quad (19)$$

Therefore, the displacement current i_1 flowing through the core from the innermost layer is:

$$i_1 = \int_0^{h_w} (U_y - U_c) C_y = \frac{U_1 + U_T - 2U_c}{2} C_{cw1} \quad (20)$$

Similarly, the displacement currents i_2, i_{31} and i_{32} flowing through the rest part of the core can be calculated as:

$$\begin{cases} i_2 = \frac{2U_1 + (2p-1)U_T - 2U_c}{2} C_{cw2} \\ i_{31} = \frac{2U_1 + (p-1)U_T - 2U_c}{2} C_{cw3} \\ i_{32} = \frac{U_1 + (p+1)U_T - 2U_c}{2} C_{cw3} \end{cases} \quad (21)$$

According to KCL law, the displacement current i_1, i_2, i_{31} and

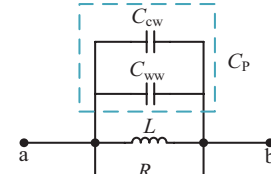


Fig. 12. Equivalent circuit of inductor.

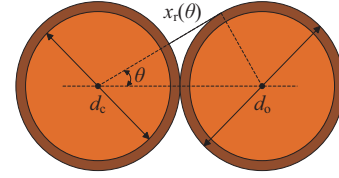


Fig. 13. Radial extension of electric field lines.

i_{32} meet the following relationship:

$$i_1 + i_2 + i_{31} + i_{32} = 0 \quad (22)$$

According to (18)–(22), the core potential U_c can be solved as:

$$U_c = U_1 + \frac{C_{cw1} + (2p-1)C_{cw2} + 2pC_{cw3}}{2C_{cw1} + 2C_{cw2} + 4C_{cw3}} U_T \quad (23)$$

Based on (18)–(23), the core potential coefficient k_U in (17) is calculated as:

$$k_U = \frac{U_d}{U_t} = \frac{U_1 - U_c}{U_t} = -\frac{C_{cw1} + (2p-1)C_{cw2} + 2pC_{cw3}}{2C_{cw1} + 2C_{cw2} + 4C_{cw3}} \quad (24)$$

By calculating the parasitic capacitance and normalization factors between each part of the core and the winding and applying (9), the total capacitance C_{cw} between the core and the winding can be obtained.

As shown in Fig. 12, since the parasitic capacitance C_{cw} and C_{ww} are gauged to the input terminals of the inductor, the parasitic capacitance C_{cw} and C_{ww} are in parallel. The total parasitic capacitance C_p of the inductor satisfies the following relationship:

$$C_p = C_{cw} + C_{ww} \quad (25)$$

IV. THE EFFECT OF ELECTRIC FIELD PATH

A. Type of Electric Field Line Model

The electric field distribution between adjacent turns affects the size of the parasitic capacitance. As shown in Fig. 3, the existing calculation method of turn-to-turn capacitance uses a straight line to represent electric field lines [15]. As shown in

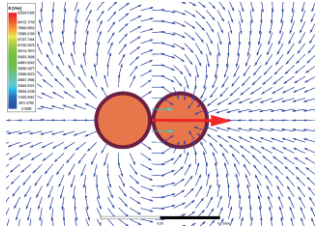


Fig. 14. Electric field line distribution of adjacent turns.

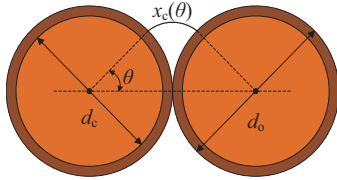


Fig. 15. Arc model of electric field line.

Fig. 13, [16] proposes an electric line model for capacitance calculations assuming that the electric field line extend in the radial direction right up to the surfaces of adjacent turn.

According to geometric analysis, the expression for the path length of this model can be derived as:

$$x_i(\theta) = d_o \left(\cos \theta \pm \sqrt{\cos^2 \theta - \frac{3}{4} - \frac{1}{2}} \right) \quad (26)$$

Fig. 14 shows the distribution of the electric field lines between adjacent turns. It can be noticed that the electric field line is not a straight line but an arc.

Comparing Figs. 13 and 14, it is clear that the simulated electric field line profiles are quite different from the straight-line assumption as well as the radial-extension assumption. Therefore, the expression in (5) and (26) cannot accurately characterize the electric field distribution between the adjacent turn. Therefore, [17] proposes an arc model to represent the distribution of the electric field line, as shown in Fig. 15.

The path length of the electric field lines for the arc model can be expressed as:

$$x_c(\theta) = \frac{d_o(1 - \cos \theta)}{2 \sin \theta} \quad (27)$$

However, compared to the simulated electric field lines shown in Fig. 14, there is a discrepancy between the arc model and the electric field lines, which lead to a large error in the calculation of the turn-to-turn capacitance. The detail comparisons will be provided in the experimental section.

The micro-arc model used in this paper is shown in Fig.16, and its corresponding expression is:

$$x_m(\theta) = \theta d_o \tan \frac{\theta}{2} \quad (28)$$

In order to verify the accuracy of these four electric

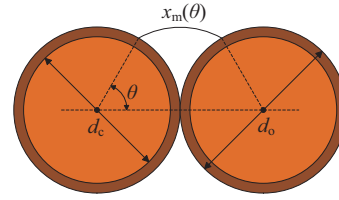


Fig. 16. Micro-arc model of electric field line.

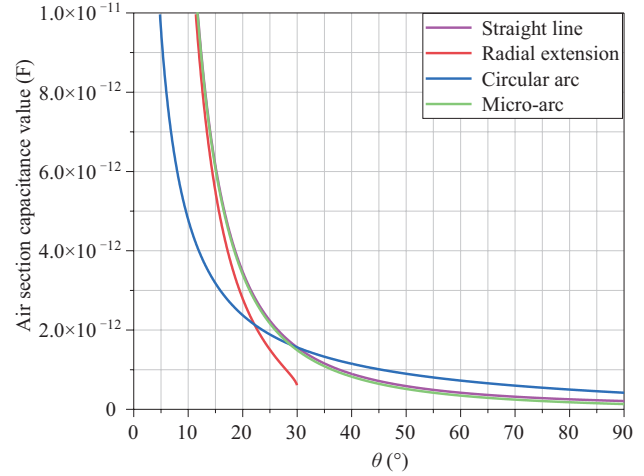


Fig. 17. Air capacitance calculation with four models.

TABLE I
COMPARISON OF CALCULATION RESULTS

Model	Calculation/pF	Simulation/pF	Relative error/%
Straight line	4.465		4.503
Radial extension Arc	3.235	4.273	24.292
Micro-arc	4.026		5.780
	4.316		0.996

field line models on the results of turn-to-turn capacitance calculations, enameled wires, with $d_o=0.34$ mm, $d_c=0.3$ mm, are used as the study object for capacitance calculations. The calculation results are shown in Fig. 17. It can find that the radial extension of electric field line model is only applicable for $0^\circ \leq \theta \leq 30^\circ$. This is because when $\theta > 30^\circ$, the electric field lines extend to infinity. The air capacitance only has a value at $0^\circ \leq \theta \leq 30^\circ$. However, compared to the simulation results shown in Fig. 14, there are electric field lines at $30^\circ < \theta \leq 90^\circ$. This leads to a large deviation.

For the arc model, it is significantly different from the other three model in the range $0^\circ \leq \theta \leq 90^\circ$. The difference between parasitic capacitance calculated by using straight line model and micro-arc model is tiny in the range of $0^\circ < \theta \leq 90^\circ$, and the accuracy between the two models needs to be further analyzed.

Table I shows the comparison results of the turn-to-turn capacitance. It can be found that the errors in the calculation results of the straight-line model and micro-arc model are

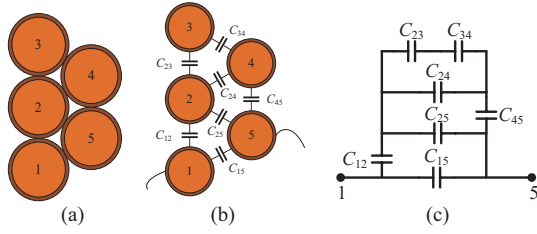


Fig. 18. Staggered winding structure. (a) Section view, (b) Turn-to-turn capacitance, (c) Equivalent circuit.

smaller than the those of the other two models, with relative errors of 4.49% and 0.99%, respectively. Since the micro-arc electric field line model represent the electric field line distribution between adjacent turns more precisely, the calculation error is smaller compared to the use of the straight-line model.

B. Impact of Integration Domain

For single-layer windings, the domain of integration chosen for the calculation of the turn-to-turn capacitance is $[-90^\circ, 90^\circ]$, which is determined by the actual electric field line distribution. For theoretical calculations, the choice of too large or too small integration domain will bring large errors to the calculation results. For multilayer staggered windings, the staggered arrangement of the conductors leads to a change in the electric field distribution between adjacent turns compared to single-layer windings. Therefore, the selection of the integration domain has a significant influence on the accuracy of the calculation results.

Fig. 18(a) shows a staggered winding structure, and with the corresponding turn-to-turn capacitance distribution shown in Fig. 18(b). Fig. 18(c) shows the equivalent circuit for the turn-to-turn capacitance.

If the integration domain is the same as that of the single-layer winding, i.e., $[-90^\circ, 90^\circ]$, the turn-to-turn capacitance is 4.465 pF. In order to verify the influence of the integration domain on the calculation results, 2D FEM simulation is used for the verification as shown in Fig. 18(a). The capacitance C_{15} given by simulation is 3.968 pF. The relative error between the calculation and the simulation is 12.5%. The error is due to the fact that coils numbered #1 and #5 are affected by coil #2, which changes the distribution of electric field between coils #1 and #5.

To minimize this part of the error, the upper part of the integration domain is $[0^\circ, 30^\circ]$, while the lower part of the integration domain is $[-90^\circ, 0^\circ]$. Therefore, when calculating the turn-to-turn capacitance between coils #1 and #5, the integration domain is chosen as $[-90^\circ, 30^\circ]$.

Based on the above considerations, the calculation result is 3.9572 pF with a relative error of 0.2611%. Similarly, Table II gives the capacitance between any two turns. According to the equivalent circuit shown in Fig.18(c), the lumped capacitance of the winding can be calculated as 6.312 pF. The simulation result is 6.299 pF. As a result, the relative error of the calculation is only 0.207%.

TABLE II
TURN-TO-TURN CAPACITANCE

Capacitor	Simulation capacitance value /pF	Calculated value/pF	Relative error /%
C_{12}	3.9454	3.9572	0.2991
C_{15}	3.9675	3.9572	0.2611
C_{23}	3.9497	3.9572	0.1901
C_{24}	3.3503	3.4489	2.4991
C_{25}	3.3486	3.4489	2.5422
C_{34}	3.9592	3.9572	0.0507
C_{45}	4.2035	4.1045	2.5093
C_{in}	6.2990	6.3120	0.2064

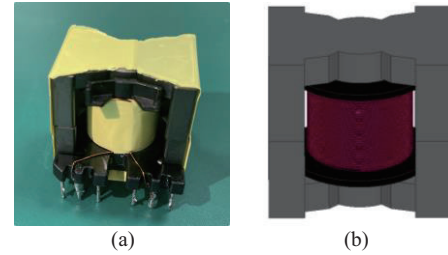


Fig. 19. Wire-wound inductor with PQ magnetic core. (a) Prototype, (b) Simulation model.

TABLE III
WINDING STRUCTURE PARAMETER

Parameter	Symbol	Unit	Value
Turns	n	-	36
Layers	p	-	1
Diameter (without insulation layer)	d_c	mm	0.3
Diameter (with insulation layer)	d_o	mm	0.34
Length of per turn	l_t	mm	47.2

If the integral domain $[-90^\circ, 90^\circ]$ is still used in the calculation of turn-to-turn capacitance, the lumped capacitance is 7.213 pF, which results in a relative error of 12.668%. Therefore, the accuracy of the proposed calculation method can be improved by 12.461%. The proposed calculation method is applicable to any winding arrangement. Hence, the calculation method is the same for the inductors with different winding methods. Besides, different winding arrangements of inductor can result in varying parasitic capacitance, but the calculation method is the same.

Based on the above analysis, the selection of the integration domain is another key factor that affects the calculation error of parasitic capacitance.

V. EXPERIMENTAL VERIFICATION

In order to verify the accuracy of the proposed parasitic capacitance calculation method, an inductor was wound as shown in Fig. 19(a) and its detail specifications are listed in Table III. Fig. 19(b) shows the simulation model of the inductor used to validate the proposed calculation method. Combining (2)–(8),

TABLE IV
CALCULATION PARAMETERS FOR MAGNETIC CORE RELATED CAPACITORS

Parameters	Symbol	Unit	Value
Radius of central column	r_1	mm	6
Distance from center axis to winding	r_2	mm	7.35
Type thickness	δ_t	mm	0.05
Relative dielectric constant of type	ϵ_t	-	3
Core window height	h_c	mm	20.55
Relative dielectric constant of bobbin	ϵ_b	-	3
Thickness of bobbin	δ_b	mm	0.67
Radius of winding	r_3	mm	7.69
Radius of side column	r_4	mm	11
Skeleton thickness	δ_v	mm	1.05
Winding height	h_w	mm	12.24

the turn-to-turn capacitance C_{tt} can be calculated to be 4.465 pF. Further, based on the energy conversion rule, the total winding capacitance C_{in} is calculated to be 0.1276 pF.

Based on the core-related parameters indicated in Fig. 8, the core-related parameters are calculated as shown in Table IV, where the weighting factors are $\alpha_{cw1}=1$, $\alpha_{cw2}=0.5$, $\alpha_{cw3}=1$. According to (9)–(24), the capacitance C_{cw} can be calculated as 0.954 pF. Further, the total parasitic capacitance of the inductor can be calculated as 1.082 pF by (25).

Manufactured inductors made of different core materials demonstrate different impedance characteristics due to different permeability. When the permeability is enough high, it only impacts the value of the inductance and it does not influence the value of parasitic capacitance. The parasitic capacitance is determined by the electric field distribution and is independent of the permeability. When the permeability is too low, the magnetic flux linkage differs between each turn of the winding is different, leading to a variation in the winding's potential distribution. In this case, the permeability affects the value of the parasitic capacitance.

In order to verify the analysis, Fig. 20 show the comparison results of the impedance characteristics under different permeability value. Table V lists the corresponding inductance and capacitance values. It can be clearly observed that as permeability increases, inductance also increases. The parasitic capacitance remains unchanged under different permeability, as shown in Fig. 20 and Table V.

For inductors with or without air gaps, the parasitic capacitances of the windings are identical in both cases. The inductance of an inductor is determined by the length of the air gap. When the permeability is sufficiently high, the magnetizing flux is far larger than the leakage flux. This means that the flux linkage each turns of the winding is the same. The voltage potential distribution across the winding remains linear and continuous unaffected by changes in air gap length.

Fig. 21 shows the impedance test platform for the tested

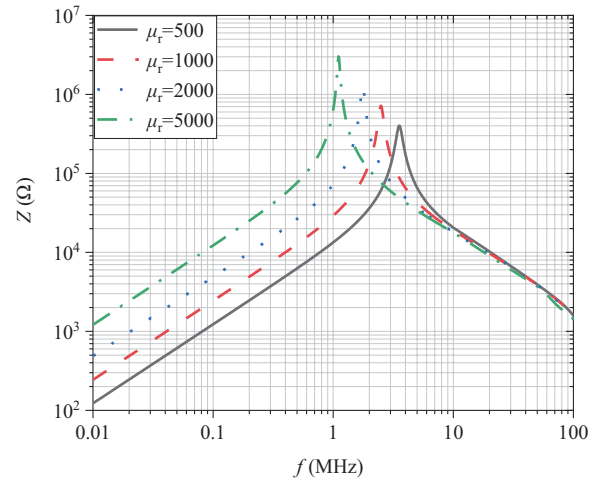


Fig. 20. Impedance characteristic versus under different permeability.

TABLE V
INDUCTANCE AND CAPACITANCE

Relative permeability	Inductance/mH	Resonant frequency/MHz	Capacitance/pF
500	1.955	3.565	1.030
1000	3.881	2.489	1.054
2000	7.736	1.754	1.064
5000	19.305	1.117	1.052

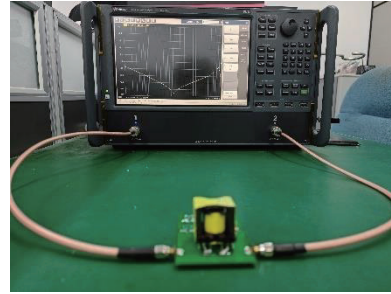


Fig. 21. Two-port test of network analyzer.

inductor, where a network analyzer, KEYSIGHT E5080A, is used to measure S -parameters and convert them into Z -parameters through post-processing. Firstly, the S -parameter test is performed under the two-port measurement in the frequency range of 100 kHz to 100 MHz. Then the impedance characteristic curve versus frequency of the inductor is obtained by converting the S -parameter to the Z -parameter.

The transformed impedance curve of the tested inductor is shown in Fig. 22 indicated by red solid line. The simulated impedance curve is also shown as green dashed line in Fig. 22. It can be found that the simulated parasitic capacitance of the inductor calculated from the resonance point location is 1.054 pF. As a result, the error between the calculated and simulated value is only 2.657%. Similarly, the measured parasitic capacitance is 1.03 pF.

As shown in Fig. 22, the resonant frequency point of the measured impedance, simulated impedance and the calculated

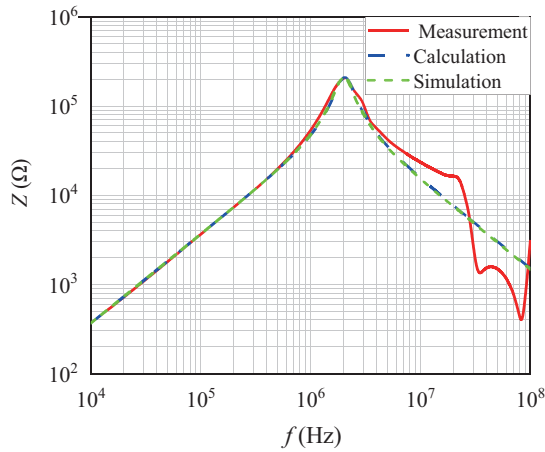


Fig. 22. Comparison of impedance curves.

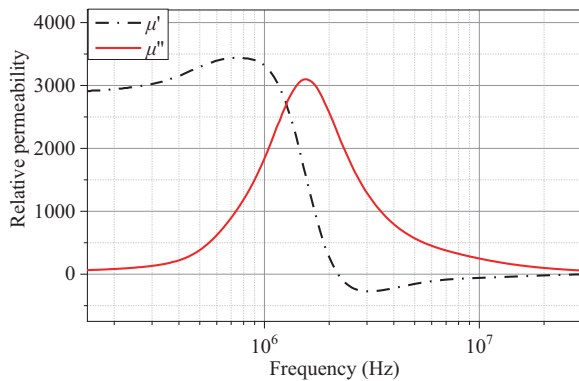


Fig. 23. Complex permeability of magnetic core.

impedance agree very well. The calculated results have a relative error 5.05% compared the measured results. Due to the unavoidable manual winding deviation during the actual winding process, the winding structure parameters of the actual inductor, such as the distance between the winding and each part of the magnetic core, the distance between the winding turns, etc., differ from the theoretical calculation results. The structure parameters of the simulation model are the same as those of the theoretical calculation. Therefore, the deviation between simulation and theoretical calculation is smaller than the deviation between measurement and theoretical calculation. The reason why the measured impedance does not conform well with the calculation results in the high frequency range is due to the influence of permeability variation with frequency. As shown in Fig. 23, it can be observed that when the frequency is higher than 1 MHz, the real portion of permeability decreases rapidly, leading to significant variations between magnetizing flux and leakage flux. Consequently, when the permeability is sufficiently low, the potential distribution along each turn is influenced by the frequency-dependent permeability. This causes parasitic capacitance variations as a function of frequency.

The proposed calculation method can be used to quickly calculate the parasitic capacitance as the calculation error is still within reasonable limits. The FEM simulation results used in

this paper is to verify the accuracy of the proposed calculation method. Compared with the FEM simulation method, the proposed calculation method has merit of computational efficiency and solution speed.

In this paper, the influence of temperature on parasitic capacitance is neglected. This is because that when the temperature is lower than curie temperature, the permeability is larger enough. For this consideration, the flux linkage each turn of the winding is the same. Then, the potential distribution along each winding can be regarded as linearly and continued. Hence, the temperature does not affect the parasitic capacitance of the inductor.

In summary, the calculation method in this paper can predict the parasitic capacitance of inductors more accurately and efficiently and guide the optimization of parasitic capacitance.

VI. CONCLUSION

This paper discusses the theoretical calculation of inductor parasitic capacitance. The conclusions are as follows.

1. The electric field distribution between adjacent turns determines the value of parasitic capacitance. A proper integral line model and integration domain can improve the accuracy of parasitic capacitance prediction.
2. The parasitic capacitance between the magnetic core and the winding is divided into several areas to calculate the total parasitic capacitance.
3. Compared with the finite element simulation, the proposed calculation method has a faster solving speed, and the error between the calculated results and the measured results is kept within 5.05%.

REFERENCES

- [1] J. He, Y. Liu, D. Bi, and X. Li, "Review of conducted electromagnetic interference suppression strategies for switching converters," in *Transactions of China Electrotechnical Society*, vol. 37, no. 6, pp. 1455–1472, Mar. 2022.
- [2] W. Shen, F. Wang, D. Boroyevich, and C. W. Tipton IV, "High-density nanocrystalline core transformer for high-power high-frequency resonant converter," in *IEEE Transactions on Industry Applications*, vol. 44, no. 1, pp. 213–222, Jan.-Feb. 2008.
- [3] Y. Gao, V. Sankaranarayanan, E. M. Dade, Y. Zhou, F. Zhou, R. W. Erickson, and D. Maksimović, "Modeling and design of high-power, high-current-ripple planar inductors," in *IEEE Transactions on Power Electronics*, vol. 37, no. 5, pp. 5816–5832, May 2022.
- [4] Y. Lan, X. Zeng, W. Chen, and Q. Chen, "High-frequency model of common-mode choke in electromagnetic interference filters," in *Transactions of China Electrotechnical Society*, vol. 40, no. 6, pp. 1–11, Mar. 2025.
- [5] L. Gao, C. Xu, G. Dong, C. Gong, and F. Zhang, "Common mode electro-magnetic interference modeling method of planar transformers based on CST software and its application," in *Transactions of China Electrotechnical Society*, vol. 35, no. 24, pp. 5057–5563, Dec. 2020.
- [6] B. Ahmad, P. Jayathurathnage, W. Martinez, and J. Kyyrä, "Parameter extraction technique for evaluation of inductive and capacitive elements of three-winding coupled inductor," in *IEEE Journal of Emerging and Selected Topics in Industrial Electronics*, vol. 3, no. 3, pp. 616–625, Jul. 2022.
- [7] G. Grandi, M. K. Kazimierzczuk, A. Massarini, and U. Reggiani, "Stray capacitances of single-layer solenoid air-core inductors," in *IEEE Transactions on Industry Applications*, vol. 35, no. 5, pp. 1162–1168, Sept.-Oct. 1999.
- [8] W. Shen, "Design of high-density transformers for high-frequency high-power converters," Ph.D. dissertation, Virginia Polytechnic Institute

and State University, 2006.

- [9] K. Nguyen-Duy, Z. Ouyang, A. Knott, and M. A. E. Andersen, "Minimization of the transformer inter-winding parasitic capacitance for modular stacking power supply applications," in *2014 16th European Conference on Power Electronics and Applications*, Lappeenranta, Finland, 2014, pp. 1–10.
- [10] A. Roch, H. Bergsma, D. Zhao, B. Ferreira, and F. Lefterink, "A new behavioural model for performance evaluation of common mode chokes," in *2007 18th International Zurich Symposium on Electromagnetic Compatibility*, Munich, Germany, 2007, pp. 501–504.
- [11] S. W. Pasko, M. K. Kazimierczuk, and B. Grzesik, "Self-capacitance of coupled toroidal inductors for EMI filters," in *IEEE Transactions on Electromagnetic Compatibility*, vol. 57, no. 2, pp. 216–223, Apr. 2015.
- [12] Qin Yu and T. W. Holmes, "A study on stray capacitance modeling of inductors by using the finite element method," in *IEEE Transactions on Electromagnetic Compatibility*, vol. 43, no. 1, pp. 88–93, Feb. 2001.
- [13] Z. De Grève, O. Deblecker, and J. Lobry, "Numerical modeling of capacitive effects in HF multiwinding transformers—part I: A rigorous formalism based on the electrostatic equations," in *IEEE Transactions on Magnetics*, vol. 49, no. 5, pp. 2017–2020, May 2013.
- [14] M. Popov, R. P. P. Smeets, L. van der Sluis, H. de Herdt, and J. Declercq, "Experimental and theoretical analysis of vacuum circuit breaker pre-strike effect on a transformer," in *IEEE Transactions on Power Delivery*, vol. 24, no. 3, pp. 1266–1274, Jul. 2009.
- [15] A. Massarini and M. K. Kazimierczuk, "Self-capacitance of inductors," in *IEEE Transactions on Power Electronics*, vol. 12, no. 4, pp. 671–676, Jul. 1997.
- [16] X. Liu, Y. Wang, J. Zhu, Y. Guo, G. Lei, and C. Liu, "Calculation of capacitance in high-frequency transformer windings," in *IEEE Transactions on Magnetics*, vol. 52, no. 7, pp. 1–4, Jul. 2016.
- [17] M. Kovacic, Z. Hanic, S. Stipetic, S. Krishnamurthy, and D. Zarko, "Analytical wideband model of a common-mode choke," in *IEEE Transactions on Power Electronics*, vol. 27, no. 7, pp. 3173–3185, Jul. 2012.



Jiangtao Tu was born in Datian, Fujian, in 2001. He is presently working towards his M.S. degree in the College of Electrical Engineering and Automation, Xiamen University of Technology, Xiamen, China. His current research interest includes electromagnetic interference in power converters.



Kaining Fu was born in Xiamen, China, in 1993. He received his M.S. and Ph.D. degrees from Fuzhou University, Fuzhou, China, in 2018 and 2021, respectively. He is presently working as a Lecturer in the College of Electrical Engineering and Automation, Xiamen University of Technology, Xiamen, China. He is a member of the Magnetic Technology Committee of the China Power of Supply Society (CPSS). His current research interests include power conversion, high-frequency magnetics, EMI debugging and solutions, and electromagnetic field analysis and applications.



Wei Chen was born in Fuzhou, China. He received his M.S. and Ph.D. degrees from Fuzhou University, Fuzhou, China, in 1987 and 1990, respectively. He worked as a Senior Visiting Professor in the Center for Power Electronics Systems (CPES), Virginia Tech, Blacksburg, Virginia, USA, from 1996 to 1998. He was with Delta Electronics Co., Ltd., as a R&D manager in the Delta Power Electronics Center, Shanghai, China, from 1999 to 2008. He has published more than 80 technical papers, including IEEE transactions and proceedings. He has held more than 40 approved patents in China and the USA. His current research interests include power conversion, high-frequency magnetic technology, EMI debugging and solutions, wireless power transfer, and electromagnetic field analysis and its applications. Professor Chen is an executive member of the council of the China Power of Supply Society (CPSS) and he served as chairman of the Magnetic Component Specialty Committee of the CPSS.



Yanhui Qiu was born in Sanming, China, in 1988, received the Ph.D. in Electrical Engineering and Automation College of Fuzhou University in 2017. He is presently working as a Lecturer in the Xiamen University of Technology in 2023. His current research interests include power electronic technology and new energy generation technology.